Accepted for J. Hydraulic Research 2014

Experimental study on the role of spanwise vorticity and vortex filaments in the outer region of open-channel flow

QIGANG CHEN, PhD Student, *Department of Hydraulic Engineering*, *Tsinghua University*, *Beijing 100084*, *China*

Email: cqg09@mails.tsinghua.edu.cn

RONALD J. ADRIAN, Regents' Professor, *School for Engineering of Matter*, *Transport and Energy*, *Arizona State University*, *Tempe*, *AZ 85287*, *USA*

Email: rjadrian@asu.edu (Corresponding Author)

QIANG ZHONG, PhD Student, *Department of Hydraulic Engineering*, *Tsinghua University*, *Beijing 100084*, *China*

Email: zhongq08@mails.tsinghua.edu.cn

DANXUN LI, Professor, *Department of Hydraulic Engineering*, *Tsinghua University*, *Beijing 100084*, *China*

Email: lidx@tsinghua.edu.cn

XINGKUI WANG, Professor, *Department of Hydraulic Engineering*, *Tsinghua University*, *Beijing 100084*, *China*

Email: wangxk@tsinghua.edu.cn

Accepted for J. Hydraulic Research 2014

Experimental study on the role of spanwise vorticity and vortex filaments in the outer region of open-channel flow

ABSTRACT

The dynamic importance of spanwise vorticity and vortex filaments has been assessed in steady, uniform open-channel flows by means of particle image velocimetry (PIV). By expressing the net force due to Reynolds' turbulent shear stress, $\partial\left(-\overline{uv}\right)/\partial y$, in terms of two velocity-vorticity correlations, $\overline{v\omega_z}$ and $\overline{w\omega_y}$, the results show that both spanwise vorticity $\overline{\omega_z}$ and the portion of it that is due to spanwise filaments make important contributions to the net force and hence the shape of the mean flow profile. Using the swirling strength to identify spanwise vortex filaments, it is found that they account for about 45% of $\overline{v\omega_z}$, the remainder coming from non-filamentary spanwise vorticity, i.e. shear. The mechanism underlying this contribution is the movement of vortex filaments away from the wall. The contribution of spanwise vortex filaments to the Reynolds stress is small because they occupy a small fraction of the flow. The contribution of the induced motion of the spanwise vortex filaments is significant.

Keywords: Hairpin vortex; net force; open-channel flow; Reynolds shear stress; spanwise vortex filament; turbulence

Running Head: Spanwise vorticity in open-channel flow

1. Introduction

Since the pioneering work of Theodorsen (1952), hairpin vortices have been hypothesized to be important coherent elements of wall turbulence. A wide body of evidence based on visualization experiments (Head and Bandyopadhyay 1981), modelling (Perry and Chong 1982, Perry *et al.* 1986, Perry and Marusic 1995, Marusic 2001), low Reynolds number direct numerical simulations (DNS) (Robinson 1991, Zhou *et al.*1996, 1999, Adrian and Liu 2002) and quantitative experiments using of particle image velocimetry (PIV) (Liu *et al.* 1991,

Meinhart and Adrian 1995, Adrian *et al.* 2000b, Christensen and Adrian 2001, Ganapathisubramani *et al.* 2003, Tomkins and Adrian 2003, Camussi and Di Felice 2006) in turbulent boundary layers and channel flows provided further evidence that hairpin vortex packets are important coherent structures in wall turbulence (Adrian 2007, Adrian and Marusic 2012). More recently, well-resolved DNS datasets in developing boundary layers (Wu and Moin 2009, Schlatter and Orlu 2012) and three-dimensional PIV experiments in boundary layers (Elsinga *et al.* 2010, Dennis and Nickels 2011) provided three-dimensional evidence of the abundance of hairpins and hairpin packets.

The theoretical model of Perry and Chong (1982) was based entirely on the hairpin vortex paradigm. In their model, the turbulent boundary layer was conceived as a random forest of self-similar hairpin-shaped vortices. These vortices originated and commenced their growth from the wall and contained all the vorticity in the flow. Later refinements of the model by Perry *et al.* (1986), Perry and Marusic (1995) and Marusic (2001) successfully reproduced many statistical quantities including mean velocity, Reynolds stress and spectra. The Reynolds stress is especially interesting as it relates the mean flow to the turbulence, and it is the "closure" term in Reynolds-averaged Navier-Stokes (RANS) equations.

Hairpin vortices have been used to qualitatively explain intense events, such as ejections and sweeps that produce most of the Reynolds shear stress (Robinson 1991, Smith *et al.* 1991). More recently, velocity fields measured by PIV made it possible to quantitatively assess the contribution of hairpins to Reynolds shear stress. Ganapathisubramani *et al.* (2003) reported the first PIV experiments to measure their contribution in a turbulent boundary layer. By measuring the velocity fields in streamwise–spanwise planes, groups of legs of hairpin vortices and associated patches of induced-motion were identified. Their results showed that the induced motions contribute about 25% to the total Reynolds shear stress while occupying only 4% of the total area. In another experiment, Wu and Christensen (2006) measured the velocity fields in streamwise–wall-normal planes of turbulent boundary layer and channel flow. They reported that the induced motion of spanwise vortex filaments contribute significantly to the total shear stress.

Much of the evidence for hairpin vortices derives from velocity vector fields and spanwise (z) vorticity fields measured on a planar slice of the flow, usually in the streamwise (x)–wall-normal (y) plane, by PIV. Roughly circular, concentrated regions of spanwise vorticity in the x-y measurement plane are interpreted to be the cross-sections of vortex filaments in the heads of the hairpins (Adrian *et al.* 2000b). The vorticity-containing filament, also called a vortex core (Chakraborty *et al.* 2005), is surrounded by inviscid, induced flow whose streamlines in the cross-sectional plane of the vortex filament are roughly circular when viewed in a coordinate system moving with its centre. It is notable that although vortex is widely taken to mean vortex filament in turbulence (Marusic and Adrian 2013), the commonly defined vortex also contains the essential characteristics of the flow induced by a vortex filament (Chakraborty *et al.* 2005). The long, thin vortex filaments are one type of vortex in a picture that also contains vortex shear layers and vortex blobs. The flows around these filaments are known to be important to the mean structure of turbulent flow. However, while filaments and patterns consistent with hairpin vortices are widely observed in two-dimensional PIV experiments, many investigators using three-dimensional DNS report difficulty in seeing the hairpin shaped filaments in three-dimensional simulations, causing some to question the significance and even the existence of hairpins (Del Alamo *et al.* 2006). The three-dimensional simulation of a boundary layer starting from laminar flow and passing through transition by Wu and Moin (2009) went far to dispel questions about hairpin existence, for their results exhibited an exceptionally clear forest of hairpins. But, questions have since been raised concerning the fate of the hairpins at larger downstream distances where the Reynolds number is larger and DNS researchers report difficulty in observing hairpins (Schlatter *et al.* 2012). Del Alamo *et al.* (2006) report only “clusters of vortices”, not hairpin packets, in channel flow, and Schlatter *et al.* (2012) see vortex legs sticking up from the wall region, but they do not see the hairpin heads connecting the legs in the downstream regions of the boundary layer, well beyond transition. They also see that the legs often appear to be one sided, i.e., a left but no right, as shown earlier by Guezennec *et al.* (1989).

The failures to see hairpin heads or missing legs may be artefacts of three-dimensional visualization of turbulent fields caused by the levels of vorticity being lower in the heads than

the legs, or in one leg versus the other, and it is conceded that visualization of well-formed packets at high Reynolds number is difficult. Even Baltzer *et al.* (2013) reported difficulty. On the other hand, there is three-dimensional visualization evidence for hairpins and hairpin packets in the work of Elsinga *et al.* (2010) and Dennis and Nickels (2011), and if one interprets the regions of compact transverse vorticity and swirling strength to be consequences of hairpins intersecting the *x*-*y* plane, then there is ample evidence for the existence of hairpins. Thus, the resolution of these conflicting observations is important to the progress of turbulence research, and it is desirable to determine the existence and significance of filamentary vortex heads using means other than qualitative visualization.

Much is known about these filamentary vortices. For example, the region just above the buffer layer is found to be densely populated with young, first generation hairpins, and their number decreases across the logarithmic layer and into the wake region (Carlier and Stanislas 2005, Wu and Christensen 2006, Pirozzoli *et al.* 2008, Stanislas *et al.* 2008, Herpin *et al.* 2010). These vortex filaments propagate on average more slowly than the mean velocity (Pirozzoli *et al.* 2008, Gao *et al.* 2011). The size of the filamentary vortices increases slowly with wall-normal position (Carlier and Stanislas 2005, Pirozzoli *et al.* 2008, Stanislas *et al.* 2008). When scaled with the local Kolmogorov length-scale, η, the mean diameter is about 8-12η (Tanahashi *et al.* 2004, Pirozzoli *et al.* 2008, Stanislas *et al.* 2008, Tanahashi *et al.* 2008, Gao *et al.* 2011, Marusic and Adrian 2013).

However, the dynamic importance of vortex filaments in wall turbulence is not fully understood. While most turbulent flow research focuses on the Reynolds shear stress, the net force per unit volume or more rigorously, the mean effect of turbulent inertia (Morrill-Winter and Klewicki 2013), is equally important. It is defined as the divergence of the Reynolds stress tensor,

$$(net\ force)_i = \frac{\partial}{\partial x_j}\left(-\rho\overline{u_i u_j}\right) \tag{1}$$

where ρ is the fluid density, and x_i, u_i, i=1,2,3 are the components of position and turbulent velocity fluctuation (i.e., deviation from the mean value). Eq. (1) offers a more direct way to understanding the importance of various structural elements. The net force appears in any

Reynolds averaged form of the mean momentum equation, where it represents the Reynolds' mean fictitious force per unit volume exerted by turbulent momentum transport on the mean flow. In the case of fully developed, parallel wall flows

$$net\ force\ in\ x\text{-}direction = \frac{\partial}{\partial y}\left(-\rho\overline{uv}\right) \tag{2}$$

where $(x, y, z)=(x_1, x_2, x_3)$, and $(u, v, w)=(u_1, u_2, u_3)$ represent the streamwise, wall-normal and spanwise components of position and velocity. Klewicki (1989) expressed the net force in this case in terms of two velocity-vorticity correlations,

$$\frac{\partial}{\partial y}\left(-\overline{uv}\right) = \overline{v\omega_z} - \overline{w\omega_y} \tag{3}$$

where ω_y and ω_z are fluctuating vorticity components in the wall-normal and spanwise directions, and the overbar denotes time averaging. Equation (3) is derived directly from the well-known vorticity form of the non-linear term in Navier-Stokes equation

$$\overline{\boldsymbol{u}\cdot\nabla\boldsymbol{u}} = \nabla\left(\frac{1}{2}\overline{u_i u_i}\right) - \overline{\boldsymbol{u}\times\boldsymbol{\omega}} \tag{4}$$

under the conditions that the streamwise and spanwise gradients of the mean turbulent kinetic energy vanish in wide, fully developed wall flows, or they can be neglected (a standard approximation for turbulent boundary layers).

The relationship in Eq. (3) shows unequivocally that spanwise vorticity and wall-normal vorticity are essential to the creation of net force. Klewicki's (1989) experiments indicated that the two velocity-vorticity correlations are roughly equal in turbulent boundary layers. Later, Klewicki *et al.* (1994) found that features of the velocity-vorticity correlations coincide well with the vortex models proposed by Falco (1991) and Smith *et al.* (1991) in the near wall region. Recently, by measuring the spectra of velocity, vorticity and their co-spectra, Priyadarshana *et al.* (2007) further established that the velocity-vorticity interactions responsible for the "scale selection" feature of the co-spectra could be interpreted properly by the hairpin vortex packets proposed by Adrian *et al.* (2000b). These authors implied a tight connection between the net force and vortex filaments in wall turbulent flows, especially the filaments that constitute hairpins and hairpin packets. But, to make this conclusion

well-grounded, it must be established that the spanwise vorticity is indeed due to filaments in order to make the association with hairpin heads.

This paper describes an investigation of the contribution of spanwise vortex filaments to net force and Reynolds stress in open-channel flow. It is intended primarily to assess the role that spanwise vorticity and its filamentary regions play in determining the net force and thereby shaping the mean velocity profile. Although filamentary vortices in open-channel flows have been observed by many PIV experiments (Roussinova *et al.* 2009, Dwivedi *et al.* 2011, Sanjou and Nezu 2011), the similarities and differences between vortices in open-channel flow and other well-documented wall turbulent flows are still unclear. Therefore, mean properties of spanwise vortex filaments in open-channel flow are also investigated and compared with results in channel flow and turbulent boundary layer flow.

The organization of this paper is as follows. In section 2, the open-channel flow facility and the PIV system used are described. The properties of the net force and its connection with spanwise vortex filaments are investigated in section 3. Contributions of spanwise vortex filaments to the Reynolds stress are analysed in section 4, and section 5 presents mean properties of spanwise vortex filaments in open-channel flow. Finally, main results and conclusions are given in section 6.

2. Experiments

2.1. *Flow facility*

Experiments are conducted in a closed-circuit tilting open-channel flume 20m long, 0.3m wide and 0.4m high. The flume has a glass bed and side-walls to facilitate velocity measurement with PIV. Five honeycombs with decreasing diameters are set at the entrance of the flume to remove large-scale structures and make the flow uniform in the transverse direction. The test section is 12m downstream of the entrance. Velocity fields are measured in a streamwise–wall-normal plane located midway between the side walls. The measurements are made under four steady, uniform flow conditions as summarized in Table1. Froude number of each case is set to be nearly the same to enable comparisons. The ratios of width to depth are at least 7.5, to ensure two-dimensionality in the central region of the flow (Nezu

2005). The friction velocity u_τ is determined based on the logarithmic law with von Karman constant κ=0.412 and additive constant A=5.29, as suggested by Nezu and Rodi (1986). A superscript + denotes quantities normalized by the friction velocity u_τ and kinematic viscosity ν.

The x-axis is oriented along the main flow, parallel to the flume bed, the y-axis is normal to the bed and pointing toward water surface, and the transverse z-axis is normal to the flume side wall with an origin at the centreline on the flume bed.

Table 1 Open-channel flow characteristics: S, bed slope; h, water depth; B, channel width; U_m, bulk mean velocity; $\mathrm{F}=U_m/\sqrt{gh}$, Froude number; $\mathrm{R}=U_m h/\nu$, Reynolds number; $\mathrm{R}_\tau=u_\tau h/\nu$, friction Reynolds number.

Case	S (-)	h (cm)	B/h (-)	U_m (cms^{-1})	u_τ (cms^{-1})	F (-)	R (-)	R_τ (-)
OCF380	0.001	2.5	12.0	25.4	1.55	0.51	5388	382
OCF490	0.001	3.0	10.0	27.8	1.68	0.51	6746	489
OCF610	0.001	3.5	8.6	30.6	1.77	0.52	8510	609
OCF740	0.001	4.0	7.5	34.4	1.91	0.55	10615	740

2.2. *Velocity measurements*

PIV is used to measure instantaneous, two-dimensional velocity vectors in the streamwise–wall-normal plane. The flow is seeded with polyamide seeding particles with a density of 1.03×10^3 kg/m^3 and a mean diameter of 5μm. The field of view is illuminated with a 1mm-thick light-sheet formed from a continuous wave laser (5W). Particle images are captured by a 2560×1920 pixel 8-bit CMOS camera with a Canon EF 50mm f/1.2 USM lens. The PIV experiment parameters are summarized in Table 2. The camera is externally triggered to sample one pair of images per second to achieve statistical independence between successive velocity fields (based on the field of view and bulk mean velocity). Within each image pair, the time interval between the first frame and the second frame is determined by the frame rate of the camera (the frame rate is adjustable when the camera is used in ROI

mode). Before the acquisition of images in each experimental case, the frame rate of the camera is adjusted according to the water velocity so that the maximum displacement of particle images from the first frame to the second frame satisfies the one-quarter rule (Adrian 1991). For each image, the exposure time is fixed to be 150μs to minimize the influence of streaking while maintaining the light intensity of particle images. A total number of 5000 image pairs are sampled in each experimental case to guarantee statistical convergence.

Particle images are analysed with a multi-pass, multi-grid window deformation method similar to that of Scarano (2002). During image interrogation, a Gaussian window-weighting function is applied automatically to avoid the effect of the edge of the interrogation window. The correlation peaks are interpolated using three-point one-dimensional Gaussian peak fitting in two dimensions. The resultant velocity fields of each iterative stage are validated using the normalized median test proposed by Westerweel and Scarano (2005), and outliers are replaced by Gaussian-kernel weighted interpolation (Adrian and Westerweel 2011). The validated velocity fields are then smoothed before the next iterative stage to prevent the possible unstable behaviour of the interrogation process (Kim and Sung 2006). The interrogation window size in the final iterative step is 16×16 pixels with 50% overlap. Inner scaled vector grid spaces, Δx^+ and Δy^+, are listed in Table 2.

Table 2 PIV experimental parameters. Δx^+=inner scaled grid space in streamwise direction; Δy^+=inner scaled grid space in wall-normal direction.

Case	Image size (pixel)	Exposure time (μs)	Frequency (Hz)	NO. of realizations	Δx^+	Δy^+
OCF380	1280×384	150	1	5000	8.1	8.1
OCF490	1280×480	150	1	5000	8.2	8.2
OCF610	1280×608	150	1	5000	8.1	8.1
OCF740	1280×720	150	1	5000	8.3	8.3

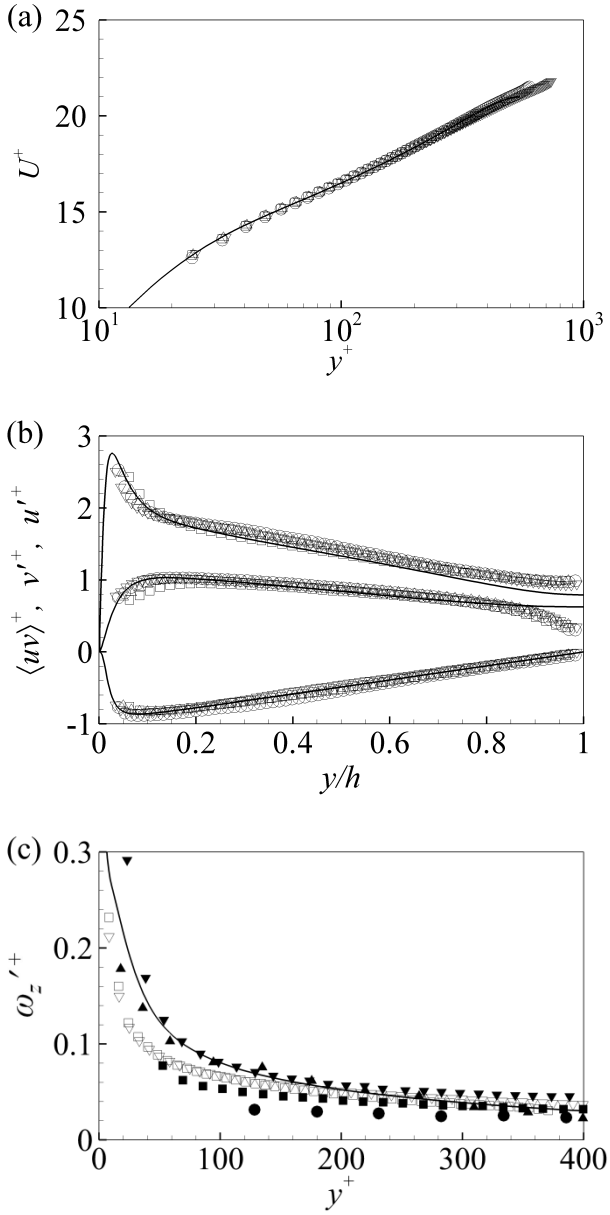

Figure 1 Profiles of (a) mean velocity, (b) turbulent intensities and Reynolds shear stress, and (c) root mean square of spanwise vorticity. □, OCF380; ▽, OCF740; —, Del Alamo *et al.* (2003), R_τ=550; ▲, Adrian *et al.* (2000), R_θ=930; ●, Adrian *et al.* (2000), R_θ=6845; ▼, Carlier and Stanislas (2005), R_θ=7500; ■, Carlier and Stanislas (2005), R_θ=7500

Since the implementation of the current PIV system is different from the standard PIV system which uses double-pulsed laser as light source, the accuracy of the measurements are firstly validated by comparing the statistics from the present measurements to those from DNS and standard PIV systems. Figures 1(a) and 1(b) present the profiles of mean velocity

and turbulent intensities/Reynolds stress, respectively. The measured results agree well with the simulated results except in the upper part of the flow where the free surface strongly influence the flow. In figure 1(c), the measured results in the near wall region are expected to be underestimated due to the inadequate wall-normal resolution of PIV measurements. But, the global agreement with the existing results is fairly good. In general, the current PIV system works quite well in resolving most of the motions especially in the outer region of the measured flows.

3. Net force and its connection with spanwise vortex filaments

3.1. *Properties of net force*

To explore the relative importance of the correlation terms involving spanwise and wall-normal vorticity in Eq. (3), the budget of net force has been calculated for each of the studied scenarios. The results of case OCF610 are presented in Fig. 2 (results of other cases are similar). The spanwise velocity and the velocity gradient components of ω_y are not measured in the present two-dimensional PIV experiments, so $\overline{w\omega_y}$ is computed from

$$\overline{w\omega_y} = u\overline{\frac{\partial v}{\partial y}} \tag{5}$$

Equation (5) can be derived by applying incompressible continuity plus the conditions of streamwise and spanwise homogeneity of the means. The reliability of Eq. (5) is verified in Fig. 2 by comparing net force computed from $\partial\langle -uv\rangle/\partial y$ (solid line) to that computed from $\langle v\omega_z\rangle - \langle u(\partial v/\partial y)\rangle$ (dash-dot line), where $\langle\cdot\rangle$ has the same meaning as an overbar. The small disparity below $y^+=60$ is caused by differentiation errors.

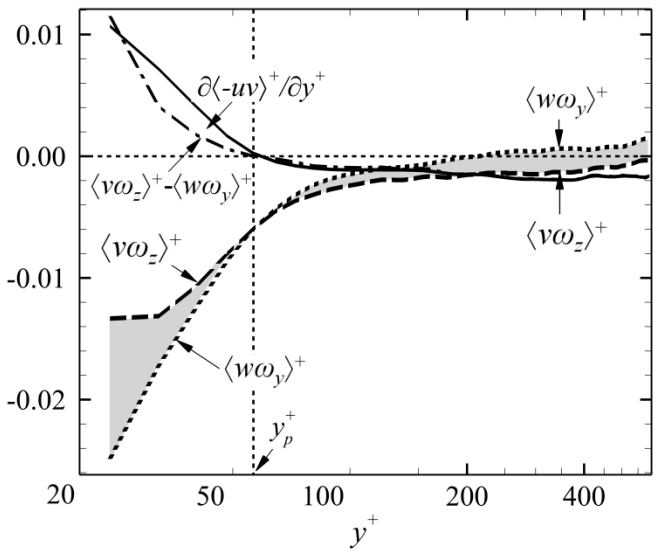

Figure 2 Budget of net force in case OCF610

In Fig. 2, the region between the curves of $\langle v\omega_z\rangle$ and $\langle w\omega_y\rangle$ is shaded to indicate the magnitude of the net force. The net force changes signs at y_p, corresponding to the location of the maximum of Reynolds stress. At y_p, the profiles of $\langle v\omega_z\rangle$ and $\langle w\omega_y\rangle$ intersect, resulting in a zero net force. In the region below y_p, the net force is positive, as $\langle w\omega_y\rangle$ exceeds $\langle v\omega_z\rangle$. Acceleration of the flow near the wall increases the mean velocity gradient at the wall and causes turbulent wall shear stress to exceed that of the laminar case. In the region above y_p, $\langle w\omega_y\rangle$ increases more quickly than $\langle v\omega_z\rangle$, leading to negative net force that reduces the mean flow velocity in the core of the flow. The behaviour of the mean velocity depends upon the delicate difference between $\langle v\omega_z\rangle$ and $\langle w\omega_y\rangle$. It may be useful to note that drag reduction can be accomplished either by making $\langle v\omega_z\rangle$ more negative, or $\langle w\omega_y\rangle$ less negative in the region below y_p. From Fig. 2 one can conclude that the features of the net force profile and the mean velocity profile would change dramatically if the contribution from $\langle v\omega_z\rangle$ were neglected. Morrill-Winter and Klewicki (2013) further demonstrated that $\langle v\omega_z\rangle$ is largely dominant over $\langle w\omega_y\rangle$ on a domain that approaches the boundary layer thickness with the increasing of Reynolds number. Thus, spanwise vorticity is essential to turbulence as we know it.

The wall-normal evolution of inner scaled $\langle v\omega_z\rangle^+$ and $\langle w\omega_y\rangle^+$ are presented as a function of y^+ in Figs. 3(a) and 3(b), respectively. In the near-wall region, $\langle v\omega_z\rangle^+$ decreases sharply in the logarithmic layer while approaching the wall (see Fig. 3(a)). This tendency is also observed in the DNS results of Crawford and Karniadakis (1997). The Reynolds number

dependency in the logarithmic region reported by Klewicki *et al.* (1994) and Priyadarshana *et al.* (2007) is not observed in the present study, possibly because the span of Reynolds number is narrow in the present study. In the outer region, $\langle v\omega_z \rangle^+$ increases slightly with wall-normal position, but remains negative. In Fig. 3(b), $\langle w\omega_y \rangle^+$ increases from a negative peak in the buffer layer and becomes slightly positive in the outer region. A similar result is also reported by Crawford and Karniadakis (1997). The Reynolds number dependence of $\langle w\omega_y \rangle^+$ is not readily observed, due to the narrow span of Reynolds number in the present study.

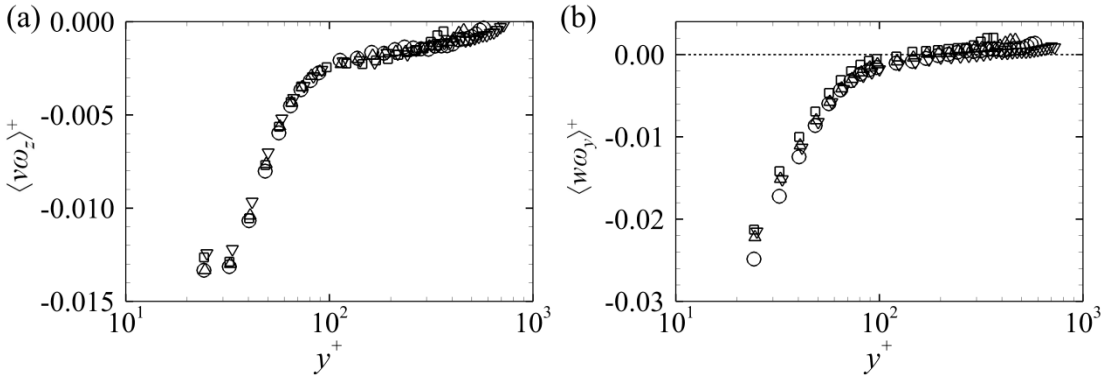

Figure 3 Profiles of inner scaled (a) $\langle v\omega_z \rangle^+$ and (b) $\langle w\omega_y \rangle^+$ versus y^+. □, OCF380; □, OCF490; ○, OCF610; □, OCF740

3.2. *Relationship between spanwise vortex filaments and net force*

A spanwise vortex filaments is identified in the *x*-*y* plane as an extremum of the swirling strength field that is surrounded by at least three points in which the swirling strength satisfies $|\Lambda_{ci}(x,y)| \geq 1.5\Lambda_{ci}^{rms}(y)$ (Wu and Christensen 2006) in both *x* and *y*. The signed swirling strength $\Lambda_{ci} = \lambda_{ci}\,\omega_z/|\omega_z|$ is used to distinguish between prograde ($\omega_z < 0$) and retrograde ($\omega_z > 0$) spanwise vortex filaments (Tomkins and Adrian 2003), where $\Lambda_{ci}^{rms}(y)$ is the root-mean-square value of Λ_{ci} at wall-normal position *y* and λ_{ci} is the imaginary part of the complex eigenvalue of the two-dimensional velocity gradient tensor (Zhou *et al.* 1999, Adrian *et al.* 2000a). Similar methods were used by Natrajan *et al.* (2007) and Herpin *et al.* (2010) to identify spanwise vortex filaments from PIV velocity fields.

An example of filamentary spanwise vortices in open-channel flow is shown in Fig. 4. Intense, concentrated regions of Λ_{ci} indicate the spanwise vortex filaments, and the velocity

vectors around these regions are plotted to confirm the swirling nature. One can observe firstly that large populations of spanwise vortex filaments exist in open-channel flow, with prograde filaments exceeding the retrograde ones in quantity. Secondly, there are more spanwise vortex filaments in the lower part of the water depth. The above features agree well with the PIV results of Wu and Christensen (2006) and Natrajan *et al.* (2007) in turbulent boundary layer and channel flow.

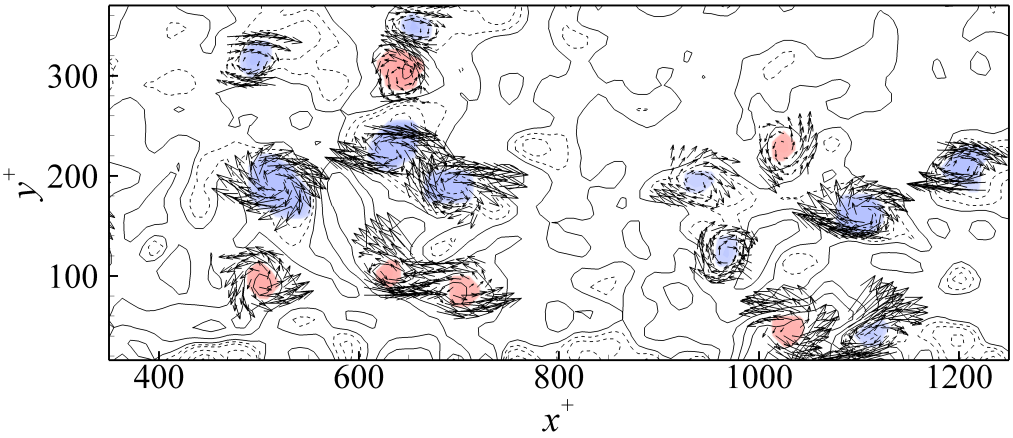

Figure 4 Example of a vortex identification result in case OCF380. Vectors denote velocity fields, local Galilean decomposition is performed; contour lines denote ω_z, and solid and dashed lines represent positive and negative values, respectively; colour contours denote Λ_{ci} within vortex cores, blue and red colour indicating prograde and retrograde vortex filaments, respectively

After spanwise vortex filaments are identified, one can see that the regions covered by spanwise vortex filaments are contained within the regions covered by spanwise vorticity. That is, spanwise vortex filaments crossing the *x*-*y* plane always have spanwise vorticity, but some portions of the regions containing spanwise vorticity do not qualify as filaments. Thus, spanwise vorticity is due to both spanwise vortex filaments and non-filamentary structures. Since spanwise vortex filaments are tightly associated with spanwise vorticity, their relationship with net force is investigated by calculating the contribution of prograde (retrograde) vortex filaments to the total mean value of $\langle v\omega_z \rangle$,

$$F_{p(r)}(y) = \frac{\sum_{i=1} v(x_i, y)\,\omega_z(x_i, y) \cdot I_{p(r)}(x_i, y)}{\sum_{i=1} v(x_i, y)\,\omega_z(x_i, y)} \quad , \tag{6}$$

where i is summed over the number of streamwise grid points in each velocity realization and the number of realizations in the ensemble. The indicator function, $I_{p(r)}$, is given as

$$I_{p(r)}(x_i, y) = \begin{cases} 1 & if\ \ (x_i, y)\ is\ within\ prograde\ \ (retrograde)\ vortex\ filaments \\ 0 & otherwise \end{cases} \tag{7}$$

It distinguishes grid points that fall within the boundary of identified vortex filaments from all others.

Figures 5(a) and 5(b) plot F_p, the contribution from prograde vortex filaments to $\langle v\omega_z \rangle$, as functions of y^+ and y/h, respectively. The contributions from the retrograde filaments F_r are plotted in Figs 5(b) and 5(d). The prograde contributions increase sharply from about zero to local maxima exceeding 60% at about y/h=0.35 and then decrease slightly within $0.35<y/h<0.85$, beyond which a sudden drop occurs. In the near wall region, profiles of F_p of each experiment collapse well when plotted versus y^+. However, the contributions from prograde vortex filaments increase with Reynolds number in the outer region of open-channel flow ($100 < y^+ < 0.8\mathrm{R}_\tau$) for fixed wall-normal position. For example, about 55%-60% of $\langle v\omega_z \rangle$ derives from prograde vortex filaments in case OCF380 compared to 60%-70% in case OCF740. In contrast to those of the prograde vortex filaments, the contributions of retrograde vortex filaments to $\langle v\omega_z \rangle$, F_r, are negative, decrease from zero to a negative peak at about y/h=0.35 and increase slightly in the region above. Within the region $y^+<100$, profiles of F_r collapse very well in wall units. In the region above, absolute percentage contributions from retrograde vortex filaments increase with Reynolds number for fixed wall-normal position. For example, the absolute percentage contribution from retrograde vortex filaments in case OCF380 is about 10% compared to 15%-20% in case OCF740. Although the absolute percentage contribution from retrograde vortex filaments is less than that from prograde ones, the fact that population of retrograde vortex filaments is only about half of prograde ones in the outer region (Carlier and Stanislas 2005, Wu and Christensen 2006, Herpin *et al.* 2010) and the intensity of spanwise vorticity within retrograde vortex filaments is weaker (Camussi

and Di Felice 2006) suggests that they are almost as efficient in net force production as prograde vortex filaments. In total, the spanwise vortex filaments contribute about 45% to $\langle v\omega_z \rangle$ while occupying only less than 9% (figures are not shown) of the total area within the region $100 < y^+ < 0.9R_\tau$. The remainder of $\langle v\omega_z \rangle$ must be attributed to sheets or blobs, or large, but weak, spanwise vortex filaments that are not identified by the present criterion.

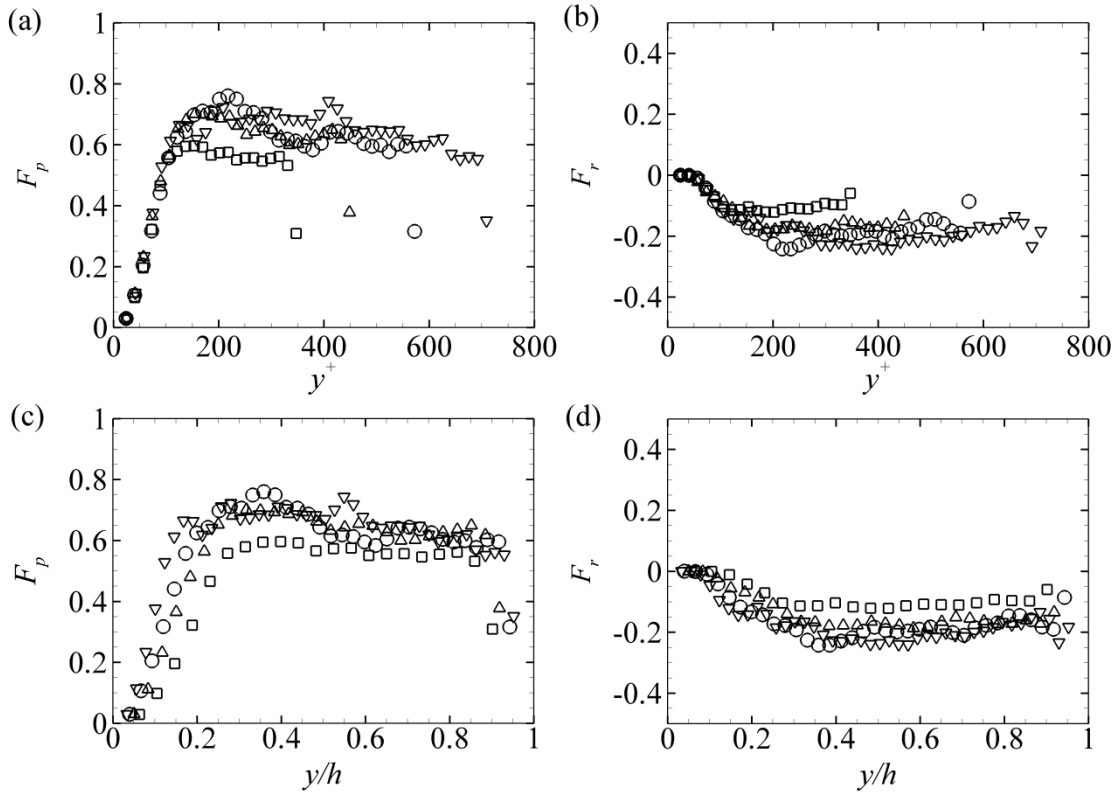

Figure 5 Fractional contributions of prograde spanwise vortex filaments to $\langle v\omega_z \rangle$. (a), (b) inner units; (c), (d) outer units.□, OCF380; △, OCF490; ○, OCF610; ▽, OCF740

The relationship of net force and spanwise vortex filaments is explored further by plotting the $v\omega_z$ field and spanwise vortex filaments of a typical velocity field simultaneously in Fig. 6. The spanwise vortex filaments are denoted by contour lines of Λ_{ci}. It is evident that nearly all identified spanwise vortex filaments are associated with concentrated $v\omega_z$ regions. Interestingly, the left half and right half of many vortex cores are covered by negative and positive $v\omega_z$, respectively. This configuration can be interpreted directly by the local velocity and vorticity field within each vortex core (see the insets). These drawings also indicate that if spanwise vortex filaments only propagate along streamwise direction, the net contribution

from them will be little. Therefore, the significant contributions presented in Fig. 5 imply that spanwise vortex filaments must move vertically while convecting with the main stream as suggested by Morrill-Winter and Klewicki (2013). Vortices covered by one-sign of $v\omega_z$ and labelled by capital letters in Fig. 6 agree well with this possibility. The positive and negative percentage contribution from prograde and retrograde vortices further suggests that most spanwise vortex filaments are likely to lift away from the wall.

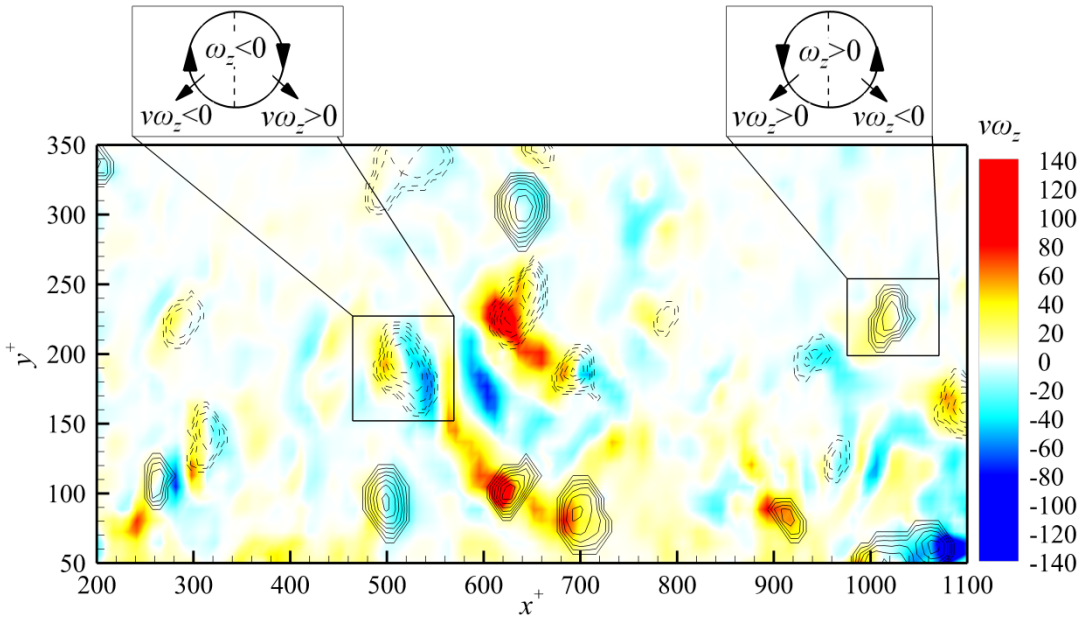

Figure 6 Spatial relationship between $v\omega_z$ field and spanwise vortex filaments in case OCF380. Colour contours represent $v\omega_z$; contour lines denote Λ_{ci} within vortex cores, solid and dashed lines represent retrograde and prograde spanwise vortex filaments, respectively

Another interesting result from Fig. 6 is that considerable regions of concentrated $v\omega_z$ exist outside the spanwise vortex filaments. The small-scale features of these regions indicate that they are mainly associated with non-filamentary small-scale structures. Therefore, while confirming the importance of spanwise vortex filaments, the present results also imply that non-filamentary small-scale structures also contribute significantly to $\langle v\omega_z \rangle$. This agrees well with the conclusions of Guala *et al.* (2006), Balakumar and Adrian (2007) and Wu *et al.* (2012) that main turbulent motions (small scale motions) contribute significantly to decelerate the flow in the region above the maximum of the Reynolds stress.

4. Contribution of spanwise vortex filaments to Reynolds stress

The contribution of spanwise vortex filaments relative to the total Reynolds stress is computed as a fraction of the total

$$S_{p(r)}(y) = \frac{-\sum_{i=1} u(x_i, y)\, v(x_i, y) \cdot I_{p(r)}(x_i, y)}{-\sum_{i=1} u(x_i, y)\, v(x_i, y)} \tag{8}$$

where the indicator function is as in Eq. (7). Figures 7(a) and 7(c) present the Reynolds-stress contribution of prograde vortex filaments, S_p, as a function of y^+ and y/h, respectively. The contributions increase quickly to a local maximum at about y^+=80 and form U-shape profiles in the region of 80 <y^+< 0.8R_τ, beyond which they decrease sharply. For fixed wall-normal position, a Reynolds-number trend is observed within 100 <y^+< 0.8R_τ, with prograde vortex filaments contributing a larger fraction to the Reynolds stress at lower Reynolds number.

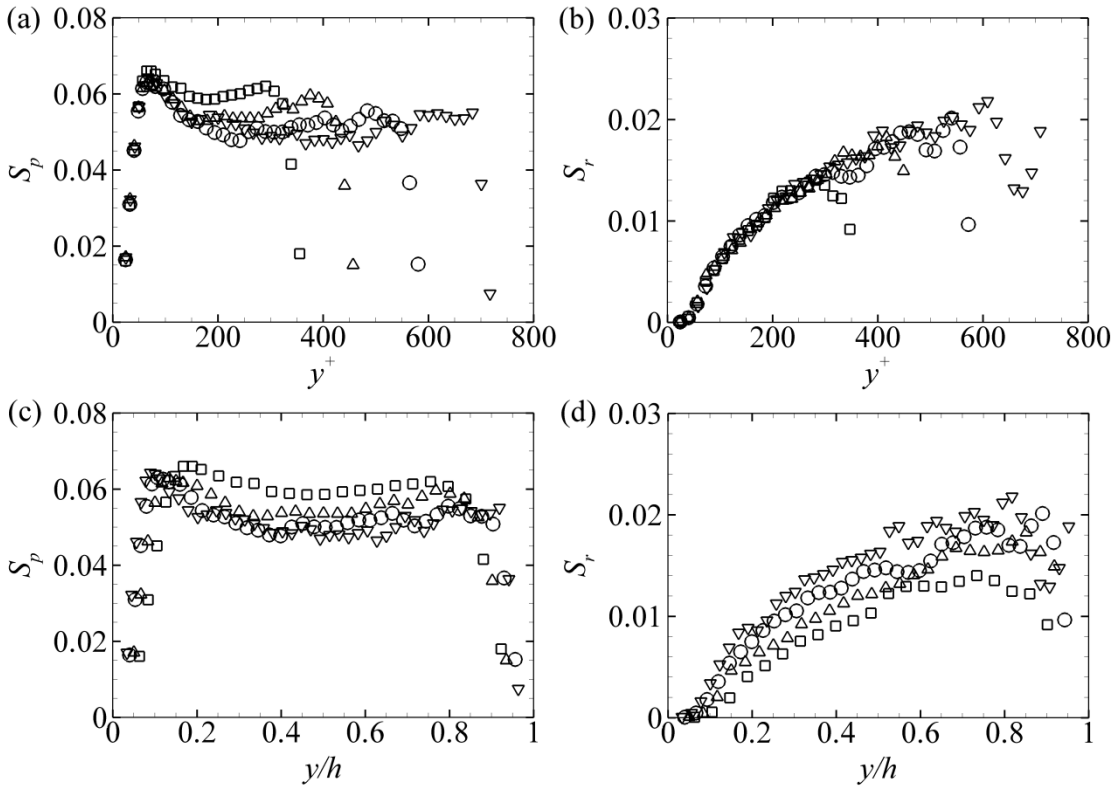

Figure 7 Fraction of Reynolds stress contained within (a, c) prograde and (b, d) retrograde vortex filaments. □, OCF380; □, OCF490; ○, OCF610; □, OCF740

In Figs. 7(b) and 7(d), the contributions of retrograde vortex filaments increase monotonically with wall-normal position within $y^+ < 0.8R_\tau$. However, a decreasing tendency is observed near the water surface. The maximum percentage contribution from retrograde vortex filaments is about 2%. When plotted versus y^+, profiles of S_r collapse well over most of the water depth. But, a Reynolds-number dependence is observed while plotted versus y/h. In general, the spanwise vortex filaments themselves contribute little to the Reynolds stress. On the other hand, the conditionally averaged Reynolds stress inside a vortex filament has a profile (not shown) only slightly less than the total Reynolds stress. Thus, the small contribution of the filaments is due to their compact size occupying a small fraction of the flow volume.

In similar experiments in a channel flow and a turbulent boundary layer, Wu and Christensen (2006) calculated the contribution of spanwise vortex filaments to the total mean shear stress (including Reynolds stress and viscous shear stress). Within the region of $0.2<y/h<0.8$, the profiles and magnitudes of their results are similar with the contributions to Reynolds stress reported in the present study. Since the viscous shear stress is negligible in this region, these similarities suggest that spanwise vortex filaments in open-channel flow, channel flow and turbulent boundary layer have similar Reynolds-stress-contribution features within $y/h<0.8$. However, different wall-normal tendencies are observed between the present open-channel flow results and the results of Wu and Christensen (2006) when approaching the outer edge of these flows.

To interpret partially why spanwise vortex filaments contribute little to the Reynolds stress, the $-uv$ field and spanwise vortex filaments of a typical velocity field (same as Fig. 4 and Fig. 6) are plotted in Fig. 8. The spanwise vortex filaments are represented by contour lines of Λ_{ci}. In comparison with the $v\omega_z$ field in Fig. 6, the patches of high instantaneous momentum flux in Fig. 8 are of a much larger scale, and most of the Reynolds stress maxima are located outside of the spanwise vortex cores. This arrangement agrees well with the idea that it is the *induced-motion* of vortex filaments that contributes significantly to the Reynolds stress (Adrian *et al.* 2000b, Ganapathisubramani *et al.* 2003, Wu and Christensen 2006), not the filaments themselves. This conclusion is further strengthened by the observation that

many vortex cores reside at the boundaries of patches of Reynolds stress with different sign, leaving them covered by negative and positive Reynolds stress simultaneously, and further reducing their contribution to Reynolds stress.

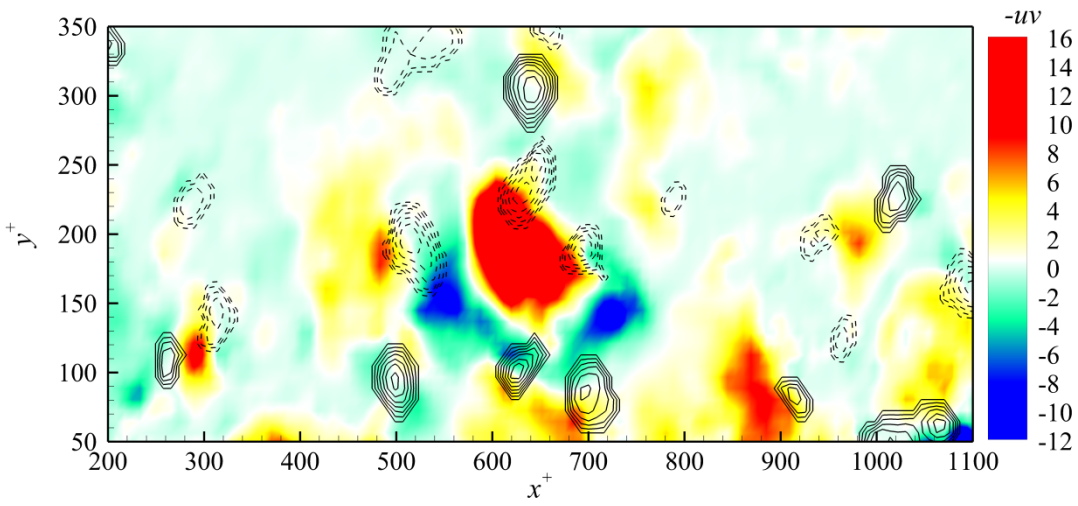

Figure 8 Spatial relationship between *-uv* field and spanwise vortex filaments in case OCF380. Colour contours represent *-uv*; contour lines denote Λ_{ci} within vortex cores, solid and dashed lines represent retrograde and prograde vortex filaments, respectively

5. Mean properties of spanwise vortex filaments

It has been shown that spanwise vortex filaments make important contributions to the net force, and that their induced-motions also play an important role in Reynolds-stress production in open-channel flow. The properties of these vortex structures are discussed in this section.

5.1. *Vortex population densities*

Following Wu and Christensen (2006), the population density of vortex filaments is defined herein as the ensemble-averaged number of prograde (retrograde) spanwise vortex filaments divided by the non-dimensional area of the sampling window in which vortical centres reside. To facilitate analysis, rectangular sampling windows are used with a wall-normal height of $3\Delta y$ and a streamwise width of L_x (equal to the streamwise field-of-view in each PIV

experiment). Given the total number of prograde (retrograde) vortex filaments residing in the sampling window centred at y, $N_{p(r)}$, the inner-scaled population density is

$$\Pi^{+}_{p(r)}(y) = \frac{N_{p(r)}(y)}{3\Delta y L_x}\left(\frac{\upsilon}{u_\tau}\right)^2 \tag{9}$$

and the outer-scaled population density is

$$\Pi^{+}_{p(r)}(y) = \frac{N_{p(r)}(y)}{3\Delta y L_x}h^2 \tag{10}$$

Figure 9 depicts the profiles of the inner- and outer-scaled population densities. Also presented in this figure are the results by Wu and Christensen (2006) of the channel flow at R_τ=1185 and the turbulent boundary layer at R_τ=1400. Figure 9(a) presents the outer-scaled population densities of prograde spanwise vortex filaments, Π_p, as a function of y/h. Similar to the observations by Wu and Christensen (2006), Π_p in open-channel flow decreases monotonically with distance from the wall in the outer region and increases with Reynolds number at fixed wall-normal positions. In Fig. 9(b), outer-scaled population densities of retrograde spanwise vortex filaments, Π_r, grow monotonically with wall-normal position until very close to the water surface. For fixed wall-normal positions, Π_r increases with Reynolds number. In Fig. 9(c) and 9(d), the wall-normal trends of the inner-scaled population densities of prograde and retrograde spanwise vortex filaments are similar to their outer-scaled counterparts, but the Reynolds-number dependence becomes obscure due to the narrow range of Reynolds number of the present study. However, when data from the channel flow and turbulent boundary layer flow are incorporated, the inner-scaled population density clearly decreases with Reynolds number. We are not sure what part of this trend is due to differences in resolution or method between the various experiments.

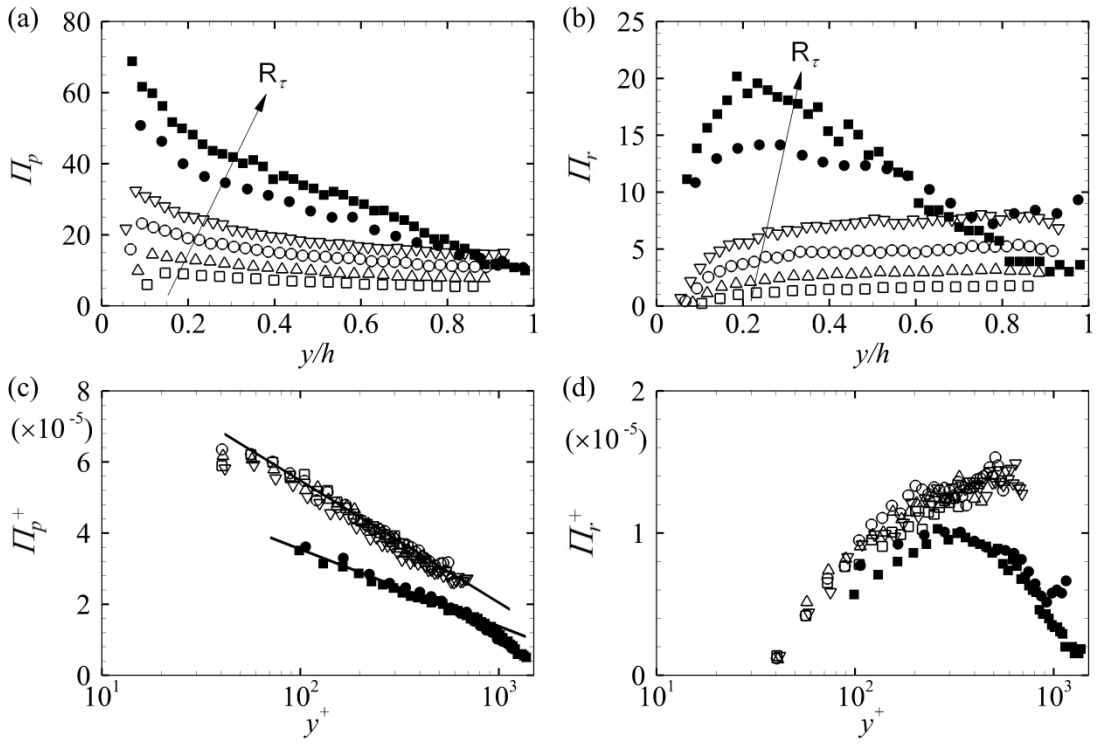

Figure 9 Profiles of population density of prograde spanwise vortex filaments (a, c) and retrograde spanwise vortex filaments (b, d). □, OCF380; △, OCF490; ○, OCF610; ▽, OCF740; ●, Wu and Christensen (2006), R_τ=1185; ■, Wu and Christensen (2006), R_τ=1400

Scrutiny of Fig. 9(c) reveals that while the general wall-normal trends are similar (monotonic decrease), disparity occurs in how Π_p^+ drops with y^+. For the open-channel flow, Π_p^+ and y^+ are linearly related in the outer region of the flow when plotted in semi-log coordinates. For the channel flow and turbulent boundary layer, however, Π_p^+ deviates from the original linear trend at about y^+=600 and then turns to a sharper decrease while approaching the outer edge of these flows. Comparing to Π_p^+, the difference in Π_r^+ becomes much more prominent as illustrated in Fig 9(d). In open-channel flow, a general increasing trend prevails in the entire flow depth; whereas in channel flow and turbulent boundary layer, the profiles of Π_r^+ follow an inverted "U" with local maximum attained at about y^+=300. The free surface in open-channel flow may partly account for these disparities as it tends to enhance the local generation of vortex filaments (Roussinova *et al*. 2009). A more plausible explanation for the difference is not immediately available.

The population trends of the vortex filaments are also computed in terms of the fraction of prograde spanwise vortex filaments that reside at a given wall-normal location

$$\Psi_p(y) = \frac{\Pi_p(y)}{\Pi_p(y) + \Pi_r(y)} \tag{11}$$

Plots of Ψ_p are presented in Figs. 10(a) and 10(b) as functions of y^+ and y/h, respectively. Predominance of prograde spanwise vortex filaments is clear, as Ψ_p is always above 0.64 in the entire flow. At given Reynolds number, Ψ_p is largest close to the channel bed, and then Ψ_p decreases with increase in y/h in the region $y/h<0.8$, beyond which Ψ_p sharply increases. At fixed y/h, Ψ_p decreases with Reynolds number. When plotted versus y^+, Ψ_p displays similarity irrespective of R_τ, with data collapsing along a single curve up to $y^+=0.8\mathsf{R}_\tau$. Such similarities were also reported in channel flow for the same range of $y^+\leq 0.8\mathsf{R}_\tau$ and in turbulent boundary layer flow for a reduced range of $y^+\leq 0.3\mathsf{R}_\tau$ (Wu and Christensen 2006). Departure from similarity occurs only in the near-free surface region where the present open-channel flow data indicate enhanced prograde vortex predominance (Ψ_p=0.7-0.8) relative to channel flow (Ψ_p<0.6) and turbulent boundary layer flow (Ψ_p=0.65) (see results by Wu and Christensen 2006).

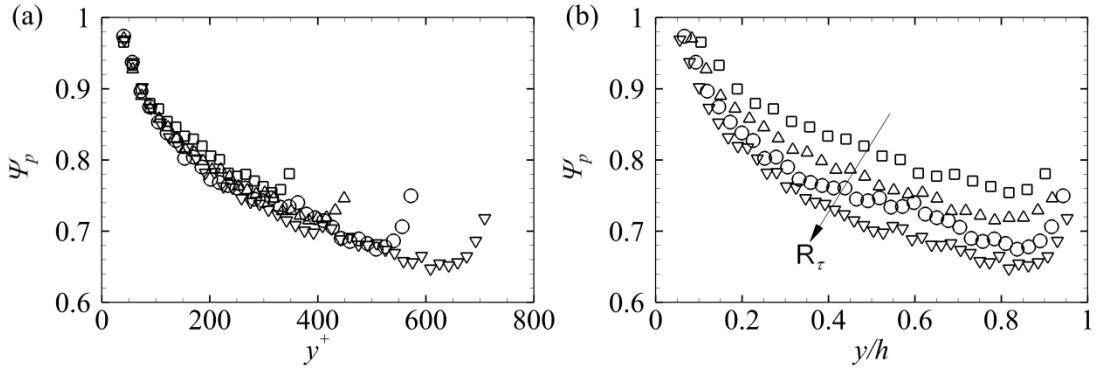

Figure 10 Proportion of prograde spanwise vortex filaments versus (a) y^+ and (b) y/h. □, OCF380; □, OCF490; ○, OCF610; □, OCF740

5.2. *Mean radius*

Quantification of vortex filament diameter depends on several factors, including choice of cross-sectional plane perpendicular to the direction of vortex filament (Gao *et al.* 2011), the

criterion for defining the vortex filament (Chakraborty *et al.* 2005), and the method of describing vortex cross-section geometry (Maciel *et al.* 2012). In the present research, the swirling strength threshold is used to determine the boundary of a vortex filament, and the radius of a vortex filament is computed as $R = \sqrt{A/\pi}$, where A is the vortex area determined by using the algorithm proposed by Gao *et al.* (2011).

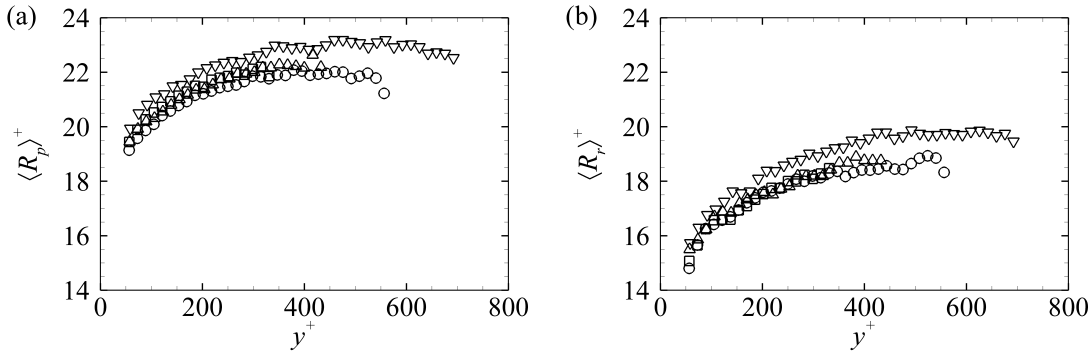

Figure 11 Mean radii of (a) prograde and (b) retrograde vortex filaments. □, OCF380; □, OCF490; ○, OCF610; □, OCF740

Figure 11 shows the inner scaled mean radius of prograde vortex filaments $\langle R_p \rangle^+$ and retrograde vortex filaments $\langle R_r \rangle^+$ as a function of y^+. The mean radius of spanwise vortex filaments increases monotonically up to y^+=0.8R_τ, suggesting that small vortices created near the wall grow as they move toward the outer region. Similar wall-normal evolution is also observed in channel flow and turbulent boundary layer flow (Carlier and Stanislas 2005, Pirozzoli *et al.* 2008, Herpin *et al.* 2010, Gao *et al.* 2011, Maciel *et al.* 2012), although the values differ somewhat among the studies, owing to the varying methods used to calculate the vortex radius as well as the way vortex radius is defined. The decreasing mean radius above y^+=0.8R_τ is believed to result from the surppression of larger vortices by the free surface. For fixed wall-normal positions, the prograde vortices are larger than retrograde vortices in agreement with Pirozzoli *et al.* (2008) and Maciel *et al.* (2012).

5.3. *Convection velocity*

The instantaneous velocity at the centre of each vortex filament is its convection velocity. Figure 12(a) presents the mean streamwise convection velocities of prograde and retrograde spanwise vortex filaments compared to the profile of mean velocity (only the results in the OCF610 case are presented, as the other cases are similar). On average, the convection

velocities of the spanwise vortex filaments are slower than the local mean velocity. This result is in agreement with the experimental findings of Adrian *et al.* (2000b), and the numerical results of Pirozzoli *et al.* (2008) and Gao *et al.* (2011). Although Carlier and Stanislas (2005) and Wu and Christensen (2006) both asserted that the spanwise vortex filaments convected with the local mean velocity on average, their experimental results showed that the convection velocity is really slightly smaller than the local mean velocity. The maximum velocity deficit, about $0.4u_{\tau,}$ appears in the range $0.2\mathrm{R}_{\tau}<y^{+}<0.5\mathrm{R}_{\tau}$.

Figure 12(b) presents the mean wall-normal convection velocities of prograde and retrograde spanwise vortex filaments. These velocities increase in the near-wall region, assume roughly constant values of about $0.2u_{\tau}$ between $100<y^{+}<400$, and then decrease in the outer region. The positive values of the mean wall-normal mean convection velocity imply that spanwise vortex filaments generally rise away from the channel bed, consistent with the concept of hairpins growing away from the wall and the idea highlighted in section 3 that the wall-normal convection of spanwise vortex filaments makes them significant to net force production. In a supersonic low Reynolds number turbulent boundary layer, Pirozzoli *et al.* (2008) reported that vertical convection velocity of retrograde spanwise vortex filaments increases monotonically from zero to about $0.4u_{\tau}$ at the outer edge of boundary layer. The difference is probably due to a flow type effect or a Reynolds number effect.

Observations of the streamwise convection velocity of prograde spanwise vortex filaments being less than the horizontal mean and upwards are fully consistent with the idea of hairpins propagating backward and upward with respect to the mean flow, due to vortex induction (Adrian *et al.* 2000b) (see the sketch in Fig. 12(a)). The backward induced motion makes a hairpin vortex convect more slowly than the surrounding flow and the upward induced motion lifts it away from the wall. Since the origion of retrograde spanwise vortex filaments in wall turbulence is still not totally clear (Natrajan *et al.* 2007), proper interpretation of their convection velocity is not attempted in the present study.

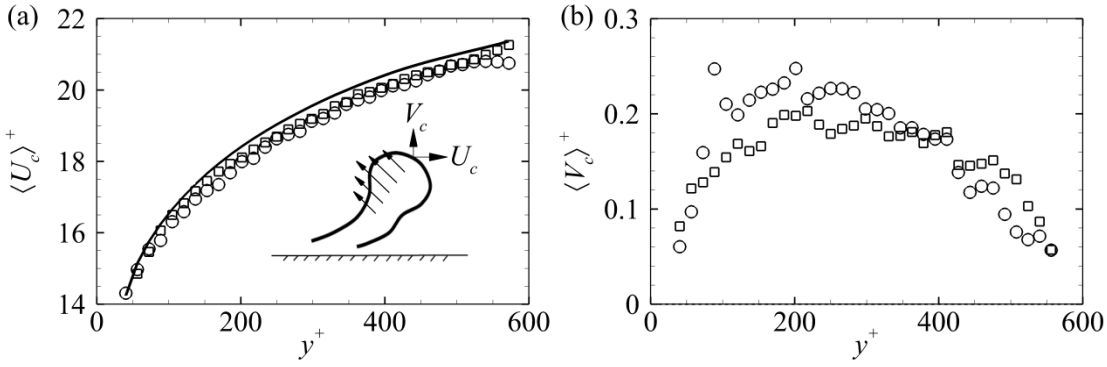

Figure 12 Profiles of mean (a) streamwise convection velocity and (b) wall-normal convection velocity of spanwise vortex filaments in case OCF610. □, prograde vortex filament; ○, retrograde vortex filament; —, mean velocity

6. Summary and Conclusions

The dynamic importance of spanwise vortex filaments and their mean properties have been measured by PIV in four steady, uniform open-channel flows with $380 \leq R_\tau \leq 740$ using a swirling-strength criterion to identify them.

Vortex filaments with spanwise vorticity are necessary to create the balance of correlation terms $\overline{v\omega_z}$ and $\overline{w\omega_y}$, that form the net force that determines the mean flow velocity profile. In the core region of open-channel flow ($100<y^+<0.9R_\tau$), at least 55% of $\overline{v\omega_z}$ is derived from prograde spanwise vortex filaments, which are commonly interpreted to be cross-sections of hairpin-vortex heads. For retrograde spanwise vortex filaments, their contribution to $\overline{v\omega_z}$ is negative and smaller in magnitude, slightly more than 10%, but still significant. Both the contributions from prograde and retrograde spanwise vortex filaments increase with Reynolds number, making a total contribution of about 45% in the region $100<y^+<0.9R_\tau$. Analysis of the velocity and vorticity fields within spanwise filaments and inspection of their convection velocities indicate that their movement away from the wall causes the significant contribution of spanwise vortex filaments to the net force.

While a broad body of evidence supports the hairpin vortex paradigm for wall turbulence, direct numerical simulations do not produce strong evidence for the existence of heads on hairpin vortices. For example, Schlatter *et al.* (2012) report only legs and necks in high Reynolds-number turbulent boundary layer. But, if this were true, then there would be no

filamentary spanwise vorticity, and the results we have measured would contradict very high quality numerical simulations. We prefer to conclude that vorticity containing heads are likely to be present in the simulations, but not as readily observed as the inclined vortex necks and legs. Perhaps failures to observe heads in some visualizations can be attributed to the vorticity in the heads being weaker than that in the legs combined with visualization using constant level contours of a vortex detection criterion such as swirling strength or the Q-criterion. Contour values that are suitable for visualizing the necks and legs may lie above the values needed to see the weaker heads.

In contrast to net force, the spanwise vortex filaments contribute little to the Reynolds stress. The contribution from prograde spanwise vortex filaments is less than 7%, and it is likely to decrease further with increasing Reynolds number. For retrograde spanwise vortex filaments, the contribution to Reynolds stress increases with wall-normal position with a maximum of 2% located at about y/h=0.8. The average Reynolds stress within the filaments is nearly the same as the local average Reynolds stress of the entire flow, so the small net contribution of the filaments must be due to the small fraction of the mean flow volume that they occupy. The spatial relationships between concentrated $-uv$ patches and spanwise vortex filaments presented here, as well as quantitative results of Ganapathisubramani *et al.* (2003) and Wu and Christensen (2006), all demonstrate that the induced motions of vortex filaments contribute much more significantly to the Reynolds stress than the vortex filaments. It is very interesting that the induced, inviscid motion is important to the Reynolds shear stress, but it is the motion of the viscous vortex filament cores that is important to the net force and, ultimately, the shape of the mean velocity profile and the wall friction. Even here, the induced fields play an important role because they are the agency causing motion of the vortex cores.

Acknowledgement

The study is financially supported by the National Natural Science Foundation of China (No.51127006) and the U. S. National Science Foundation under Grant No. CBET-0933848.

Notation

η	=	Kolmogorov micro-scale (m)
$\lambda_{ci}, \Lambda_{ci}$	=	swirling strength (s^{-1})
$\Pi_p, \Pi_r, \Pi_p^+, \Pi_r^+$	=	population densities of spanwise vortex filament (-)
ρ	=	fluid density (kg m^{-3})
ν	=	kinematic viscosity (m^2 s^{-1})
Ψ_p	=	fraction of prograde spanwise vortex filament (-)
ω_y, ω_z	=	vorticity fluctuation (s^{-1})
B	=	channel width (m)
$\Delta x^+, \Delta y^+$	=	inner-scaled grid space (-)
F	=	Froude number (-)
F_p, F_r	=	contribution of vortex filaments to the net force (-)
h	=	water depth (m)
L_x	=	streamwise field-of-view of PIV measurement (m^{-1})
N_p, N_p	=	number of vortex filament (-)
R	=	Reynolds number (-)
R_τ	=	friction Reynolds number (-)
R_p, R_r	=	radius of spanwise vortex filament (m)
S	=	bed slope (-)
S_p, S_r	=	contribution of spanwise vortex filaments to the Reynolds stress (-)
$(u, v, w)=(u_1,u_2,u_3)$	=	velocity fluctuation (m s^{-1})
u_τ	=	friction velocity(m s^{-1})
U_c, V_c	=	convection velocity of vortex filament (m s^{-1})
$(x, y, z)= (x_1,x_2,x_3)$	=	position (m)

References

Adrian, R.J. (1991). Particle-imaging techniques for experimental fluid mechanics. *Ann. Rev. Fluid Mech*. 23(1), 261-304.

Adrian, R.J. (2007). Hairpin vortex organization in wall turbulence. *Phys. Fluids.* 19, 041301.

Adrian, R.J., Christensen, K.T., Liu, Z.C. (2000a). Analysis and interpretation of instantaneous turbulent velocity fields. *Exp. Fluids.*29, 275-290.

Adrian, R.J., Liu, Z. (2002). Observation of vortex packets in direct numerical simulation of fully turbulent channel flow. *J.Visual.*5(1), 9-19.

Adrian, R.J., Marusic, I. (2012). Coherent structures in flow over hydraulic engineering surfaces. *J. Hydraulic Res.* 50(5):451-464.

Adrian, R.J., Meinhart, C.D., Tomkins, C.D. (2000b). Vortex organization in the outer region of the turbulent boundary layer. *J. Fluid Mech.* 422(1), 1-54

Adrian, R.J., Westerweel, J. (2011).*Particle image velocimetry*. Cambridge University Press, New York.

Balakumar, B., Adrian, R.J. (2007). Large-and very-large-scale motions in channel and boundary-layer flows. *Phil. Trans. R. Soc. A.* 365, 665-681.

Baltzer, J.R., Adrian, R.J., Wu, X.H. (2013). Structural organization of large and very large scales in turbulent pipe flow simulation. *J. Fluid Mech.*720, 236-279.

Camussi, R., Di Felice, F. (2006). Statistical properties of vortical structures with spanwise vorticity in zero pressure gradient turbulent boundary layers. *Phys. Fluids.* 18,035108.

Carlier, J., Stanislas, M. (2005). Experimental study of eddy structures in a turbulent boundary layer using particle image velocimetry. *J. Fluid Mech.* 535(36),143-188.

Chakraborty, P., Balachandar, S., Adrian, R.J. (2005). On the relationships between local vortex identification schemes.*J. Fluid Mech.* 535(1), 189-214.

Christensen, K., Adrian, R.J. (2001). Statistical evidence of hairpin vortex packets in wall turbulence. *J. Fluid Mech.* 431(1), 433-443.

Crawford, C.H., Karniadakis, G.E. (1997). Reynolds stress analysis of EMHD-controlled wall turbulence. Part I. Streamwise forcing. *Phys. Fluids.* 9(3),788-806.

Del Alamo, J.C., Jimenez, J., Zandonade, P., Moser, R.D.(2006). Self-similar vortexclusters in the turbulent logarithmic region. *J. Fluid Mech.* 561, 329-358.

Dennis, D.J.C., Nickels, T.B. (2011). Experimental measurement of large-scale three-dimensional structures in a turbulent boundary layer. Part 1. Vortex packets. *J. Fluid Mech.*673(1), 180-217.

Dwivedi, A., Melville, B.W., Shamseldin, A.Y., Guha, T.K. (2011). Flow structures and hydrodynamic force during sediment entrainment. *Water Resour. Res.* 47, W01509.

Elsinga, G., Adrian, R.J., Van Oudheusden, B., Scarano, F. (2010). Three-dimensional vortex organization in a high-Reynolds-number supersonic turbulent boundary layer. *J. Fluid Mech.* 644(1),35-60.

Falco, R.E. (1991). A coherent structure model of the turbulent boundary layer and its ability to predict Reynolds number dependence. *Phil. Trans. R. Soc. Lond. A.* 336, 103-129.

Ganapathisubramani, B., Longmire, E.K., Marusic, I. (2003). Characteristics of vortex packets in turbulent boundary layers. *J. Fluid Mech.* 478, 35-46.

Gao, Q., Ortiz-Dunnas, C., Longmire, E.K. (2011). Analysis of vortex populations in turbulent wall-bounded flows. *J. Fluid Mech.* 678, 87-123.

Guala, M., Hommema, S., Adrian, R.J. (2006). Large-scale and very-large-scale motions in turbulent pipe flow. *J. Fluid Mech.*554(1),521-542.

Guezennec, Y.G., Piomelli U., Kim J. (1989). On the shape and dynamics ofwall structures in turbulent channel flow. *Phys. Fluids A.*1(4), 764-766.

Hambleton, W., Hutchins, N., Marusic, I. (2006). Simultaneous orthogonal-plane particle image velocimetry measurements in a turbulent boundary layer. *J. Fluid Mech.* 560,53-64.

Head, M., Bandyopadhyay, P. (1981). New aspects of turbulent boundary-layer structure. *J. Fluid Mech.* 107, 297-338.

Herpin, S., Stanislas, M., Soria, J. (2010). The organization of near-wall turbulence: a comparison between boundary layer SPIV data and channel flow DNS data. *J. Turbulence.*11(47), 1-30.

Kim B.J., Sung H.J. (2006). A further assessment of interpolation schemes for window deformation in PIV. *Exp. in Fluids.*41 (3), 499-511.

Klewicki, J.C. (1989). Velocity-vorticity correlations related to the gradients of the Reynolds stresses in parallel turbulent wall flows. *Phys. Fluids A.* 1(7), 1285-1288.

Klewicki, J.C., Murray, J., Falco, R. (1994). Vortical motion contributions to stress transport in turbulent boundary layers. *Phys. Fluids.*6(1), 277-286.

Kuo, A.Y.S., Corrsin, S. (1972). Experiment on the geometry of the fine-structure regions in fully turbulent fluid. *J. Fluid Mech.* 56(3), 447-479.

Liu, Z.C., Landreth, C., Adrian, R.J., Hanratty, T. (1991). High resolution measurement of turbulent structure in a channel with particle image velocimetry. *Exp. Fluids.* 10 (6), 301-312.

Maciel,Y., Robitaille, M., Rahgozar, S. (2012). A method for characterizing cross-sections of vortices in turbulent flows. *Int. J. heatfluid fl.* 37, 177-188.

Marusic, I. (2001). On the role of large-scale structures in wall turbulence. *Phys. Fluids.* 13, 735-743.

Marusic, I. Adrian, R.J. (2013). The eddies and scales of wall turbulence. In *Ten chapters in turbulence*. P.A. Davidson, Y. Kaneda, K.R. Sreenivasan, eds. Cambridge University Press, New York.

Meinhart, C.D., Adrian, R.J. (1995). On the existence of uniform momentum zones in a turbulent boundary layer. *Phys. Fluids.*7(4), 694-696.

Morrill-Winter, C., Klewicki, J. (2013). Influences of boundary layer scale separation on the vorticity transport contribution to turbulent inertia. Phys. Fluids. 25(1), 015108.

Natrajan,V.K., Wu,Y., Christensen, K.T. (2007). Spatial signatures of retrograde spanwise vortices in wall turbulence. *J. Fluid Mech.* 574, 155-168.

Nezu, I. (2005). Open-channel flow turbulence and its research prospect in the 21st century. *J. Hydraulic Eng.* 131, 229-246.

Nezu, I., Rodi, W. (1986). Open-Channel Flow Measurements with a Laser Doppler Anemometer. *J. Hydraulic Eng.* 112(5), 335-355.

Perry, A., Chong, M. (1982). On the mechanism of wall turbulence.*J. Fluid Mech.* 119 (173), 106-121.

Perry, A., Henbest, S., Chong, M. (1986). A theoretical and experimental study of wall turbulence. *J. Fluid Mech.* 165 (1), 163-199.

Perry, A., Marusic, I. (1995). A wall-wake model for the turbulence structure of boundary layers. Part 1. Extension of the attached eddy hypothesis. *J. Fluid Mech.* 298, 361-388.

Pirozzoli, S., Bernardini, M., Grasso, F. (2008). Characterization of coherent vortical structures in a supersonic turbulent boundary layer. *J. Fluid Mech.*613, 205-231.

Pirozzoli, S., Bernardini, M., Grasso, F. (2010). On the dynamical relevance of coherent vortical structures in turbulent boundary layers. *J. Fluid Mech.* 648, 325-349.

Priyadarshana, P., Klewicki, J.C., Treat, S., Foss, J. (2007). Statistical structure of turbulent-boundary-layer velocity-vorticity products at high and low Reynolds numbers. *J. Fluid Mech.* 570, 307-346.

Robinson, S.K. (1991). Coherent motions in the turbulent boundary layer. *Ann. Rev. Fluid Mech*.23(1), 601-639.

Roussinova, V., Shinneeb, A.M., Balachandar, R. (2009). Investigation of fluid structures in a smooth open-channel flow using proper orthogonal decomposition. *J. Hydraulic Eng.*136 (3),143-154.

Sanjou, M., Nezu, I. (2011). Turbulence structure and coherent vortices in open-channel flows with wind-induced water waves. *Environ. Fluid Mech.* 11 (2):113-131.

Scarano, F. (2002). Iterative image deformation methods in PIV. *Meas. Sci. Technol.* 13, R1-R19.

Schlatter, P., Orlu, R. (2012). Turbulent boundary layers at moderate Reynolds numbers: inflow length and tripping effects. *J. Fluid Mech.*710, 5-34.

Schlatter, P., Orlu, R., Li, Q., Hussain, F., Henningson, D. (2012). On the near-wall vortical structures at high Reynolds numbers. *B. Am. Phys. Soc.*, 57.

Smith, C.R., Walker, J., Haidari, A., Sobrun, U. (1991). On the dynamics of near-wall turbulence. *Phi. Trans. R. Soc. Lond. A.* 336,131-175.

Stanislas, M., Perret, L., Foucaut, J.M. (2008). Vortical structures in the turbulent boundary layer: a possible route to a universal representation. *J. Fluid Mech.* 602, 327-382.

Tanahashi, M., Hirayama, T., Taka, S., Miyauchi, T. (2008). Measurement of fine scale structure in turbulence by time-resolved dual-plane stereoscopic PIV. *Int. J. heatfluid fl.* 29(3), 792-802.

Tanahashi, M., Kang, S.J., Miyamoto, T., Shiokawa, S., Miyauchi, T. (2004). Scaling law of fine scale eddies in turbulent channel flows up toRe_τ= 800. *Int. J. heatfluid fl.* 25(3), 331-340.

Theodorsen, T.(1952). Mechanism of turbulence. Proc. 2nd Midwestern Conf. *Fluid Mechanics*, 1-19, Ohio State University, Columbus.

Tomkins, C.D., Adrian, R.J. (2003). Spanwise structure and scale growth in turbulent boundary layers. *J. Fluid Mech.* 490, 37-74.

Westerweel, J., Scarano, F. (2005). Universal outlier detection for PIV data. *Exp. Fluids.* 39(6), 1096-1100.

Wu, X.H., Moin, P. (2009).Direct numerical simulation of turbulence in a nominally zero-pressure-gradient flat-plate boundary layer.*J. Fluid Mech.*630, 5-41.

Wu, X.H., Baltzer, J.R., Adrian, R.J. (2012). Direct numerical simulation of a 30R long turbulent pipe flow at R^+=685: large- and very large-scale motions. *J. Fluid Mech.* 698, 235-28.

Wu, Y., Christensen, K.T. (2006). Population trends of spanwise vortices in wall turbulence. *J. Fluid Mech.* 568 (1), 55-76.

Zhou, J., ,Adrian, R.J., Balachandar, S. (1996). Autogeneration of near wall vortical structures in channel flow. *Phys. Fluids.* 8,288-291.

Zhou, J., Adrian, R.J., Balachandar, S., Kendall, T. (1999). Mechanisms for generating coherent packets of hairpin vortices in channel flow.*J. Fluid Mech.*387 (1):353-396